Available online at www.sciencedirect.com
ScienceDirect
Catalysis Today 119 (2007) 64–72
CATALYSIS TODAY
www.elsevier.com/locate/cattod

Transient behaviour of catalytic monolith with NO_x storage capacity

Petr Kočí [a,c], Matyáš Schejbal [a,c], Jan Trdlička [a,c], Tomáš Gregor [a,c], Milan Kubíček [b,c], Miloš Marek [a,c,*]

[a] Department of Chemical Engineering, Prague Institute of Chemical Technology, Technická 5, CZ-166 28 Praha, Czech Republic
[b] Department of Mathematics, Prague Institute of Chemical Technology, Technická 5, CZ-166 28 Praha, Czech Republic
[c] Center for Nonlinear Dynamics of Chemical and Biological Systems, Prague Institute of Chemical Technology, Technická 5, CZ-166 28 Praha, Czech Republic

Available online 15 September 2006

Abstract

Transient behaviour of catalytic monolith converter with NO_x storage is studied under conditions typical for automobiles with lean-burn engines (i.e., diesel and advanced gasoline ones). Periodical alternation of inlet concentrations is applied—NO_x are adsorbed on the catalyst surface during a long reductant-lean phase (2–3 min) and then reduced to N_2 within a short reductant-rich phase (2–6 s). Samples of industrial NO_x storage and reduction catalyst of NM/Ba/CeO_2/γ-Al_2O_3 type (NM = noble metal), washcoated on 400 cpsi cordierite substrate, are used in the study. Effects of the rich-phase length and composition on the overall NO_x conversions are examined experimentally. Reduction of NO_x by CO, H_2 and unburned hydrocarbons (represented by C_3H_6) in the presence of CO_2 and H_2O is considered.

Effective, spatially 1D, heterogeneous mathematical model of catalytic monolith with NO_x and oxygen storage capacity is described. The minimum set of experiments needed for the evaluation of relevant reaction kinetic parameters is discussed: (i) CO, H_2 and HC oxidation light-off under both lean and rich conditions, including inhibition effects, (ii) NO/NO_2 transformation, (iii) NO_x storage, including temperature dependence of effective NO_x storage capacity, (iv) water gas shift and steam reforming under rich conditions, i.e., *in situ* production of hydrogen, (v) oxygen storage and reduction, including temperature dependence of effective oxygen storage capacity, and (vi) NO_x desorption and reduction under rich conditions. The experimental data are compared with the simulation results.

Keywords: NO_x storage; NO_x reduction; Catalyst; Monolith; Automobile exhaust gas; Mathematical modeling

1. Introduction

Classical gasoline engines in automobiles are operated at stoichiometric air/fuel ratio. Under such conditions, it is possible to abate harmful exhaust gas components in three-way catalytic converter (TWC), where the oxidation of CO and unburned hydrocarbons (HC) and the reduction of nitrogen oxides (NO_x) take place simultaneously. On the contrary, economical diesel and advanced gasoline (lean-burn) engines are operated with excess of air in fuel mixture, which results in high O_2 concentrations in the exhaust gas and complicated NO_x abatement. Special exhaust gas converters and/or advanced management of combustion in the engine are then needed for the reduction of the NO_x emissions. In the NO_x storage and reduction catalyst (NSRC) [1], the NO_x are adsorbed on the catalyst surface during a longer reductant-lean phase (several minutes), and then reduced within a short (several seconds) reductant-rich phase, realised, e.g., by special fuel injection and/or exhaust gas recirculation management [2].

The NO_x storage in the form of surface nitrites and nitrates on active Ba sites is a complex process, in which different adsorption mechanisms take part simultaneously under oxidising conditions. The process is influenced by the NO oxidation to NO_2, by the transformation of different forms of the stored NO_x (nitrites, nitrates), by the competitive chemisorption of other gases (CO_2, H_2O, SO_2), by the presence of different types of NO_x storage sites, and by the internal diffusion effects—cf., e.g., [3–9] and the review [10].

Abbreviations: GHSV, gas hourly space velocity (h^{-1}); HC, hydrocarbons; NM, noble metals; NSRC, NO_x storage and reduction catalyst

* Corresponding author at: Department of Chemical Engineering, Prague Institute of Chemical Technology, Technická 5, CZ-166 28 Praha, Czech Republic. Tel.: +420 22044 3104; fax: +420 22044 4320.
E-mail addresses: petr.koci@vscht.cz (P. Kočí), milos.marek@vscht.cz (M. Marek).
URL: http://www.vscht.cz/monolith

0920-5861/$ – see front matter © 2006 Elsevier B.V. All rights reserved.
doi:10.1016/j.cattod.2006.08.014

Nomenclature

a	density of external surface area in monolith ($m^2\ m^{-3}$)
A	pre-exponential factor of reaction, dimension depends on the reaction
c	concentration in bulk gas ($mol\ m^{-3}$)
c^s	concentration in washcoat pores ($mol\ m^{-3}$)
c_p^g	specific heat capacity of gas ($J\ kg^{-1}\ K^{-1}$)
c_p^s	effective specific heat capacity of solid phase ($J\ kg^{-1}\ K^{-1}$)
E_a	activation energy of reaction ($J\ mol^{-1}$)
F	moles flow rate ($mol\ s^{-1}$)
ΔH_r	standard reaction enthalpy ($J\ mol^{-1}$)
J	number of reactions
k	kinetic constant of reaction, dimension depends on the reaction
k_c	mass transfer coefficient ($m\ s^{-1}$)
k_h	heat transfer coefficient ($J\ m^{-2}\ K^{-1}\ s^{-1}$)
K	number of gas components
K_a	inhibition constant
K_y^{eq}	thermodynamic equilibrium constant, 1
L	length of monolith (m)
M	number of surface-deposited components
R	reaction rate ($mol\ m^{-3}\ s^{-1}$) (related to washcoat volume)
R^g	universal gas constant ($8.31434\ J\ mol^{-1}\ K^{-1}$)
S	frontal area of monolith (m^2)
t	time (s)
T	temperature of gas (K)
T^s	temperature of solid phase (K)
T^e	temperature of surroundings (K)
v	linear gas velocity ($m\ s^{-1}$)
V	volume (m^3)
$\dot{V}$	volumetric flow rate ($m^3\ s^{-1}$)
y	mole fraction of gas component, 1
z	spatial coordinate along monolith (m)

Greek letters

α	effective heat exchange coefficient ($J\ m^{-3}\ K^{-1}\ s^{-1}$)
ε^g	fraction of open frontal area in monolith, 1
ε^s	porosity of washcoat, 1
φ^s	volume fraction of active washcoat in entire solid phase, 1
ν	stoichiometric coefficient, 1
ρ^g	gas density ($kg\ m^{-3}$)
ρ^s	effective density of solid phase (incl. pores) ($kg\ m^{-3}$)
ψ	relative surface concentration of stored component, 1
Ψ_{cap}	storage capacity ($mol\ m^{-3}$) (related to washcoat volume)

Subscripts

j	index of reaction
k	index of gas component
m	index of surface-deposited component

Superscripts

eq	equilibrium
exp	experiment
g	gas
in	inlet
out	outlet
s	solid phase (washcoat and monolith substrate)
sim	simulation
w	washcoat

The stored NO_x (i.e., surface nitrites and nitrates) decompose at higher temperatures and/or excess of reducing components (CO, HC and H_2), the latter condition being necessary for an efficient reduction of the released NO_x. The processes within the short rich phase are highly transient, involving internal transport effects, interactions between NO_x storage components, catalytic noble metals and oxygen storage materials [10]. Exothermic effects also play very important role in the practical application, i.e., under nearly adiabatic conditions [11].

In this paper we present an effective, spatially 1D, heterogeneous mathematical model of catalytic monolith, which is able to describe and quantify the most important effects taking place in the course of typical periodic operation of NO_x storage and reduction catalysts in automobiles—catalyst light-off for CO, H_2 and HC oxidation including inhibition effects, water gas shift and steam reforming reactions, temperature-dependent oxygen and NO_x storage, and the effects of rich-phase length and compostion (CO, H_2 or HC). Minimum set of experiments necessary for the evaluation of relevant reaction-kinetics parameters is discussed and examples of the experimental results are given.

2. Mathematical model of NSRC monolith

Spatially pseudo-1D, heterogeneous model of monolith channel with plug-flow and surface deposition of gas components is employed in the simulations [12]. The following balances are considered: mass balances in the flowing gas, including accumulation, convection, and external mass transfer (1); mass balances in the washcoat pores, including accumulation, external mass transfer, and catalytic reactions (2); mass balances on the catalyst surface, including accumulation, and catalytic reactions (3); enthalpy balance of the flowing gas, including accumulation, convection, and gas-solid heat transfer (4); enthalpy balance of the solid phase, including accumulation, axial heat conduction, gas-solid heat transfer, heat exchange with the surroundings, and heat source from catalytic reactions (5):

$$\frac{\partial c_k(z,t)}{\partial t} = -\frac{\partial (v c_k)}{\partial z} + \frac{k_c a}{\varepsilon^g}(c_k^s - c_k), \qquad k = 1,\ldots,K \tag{1}$$

$$\frac{\partial c_k^s(z,t)}{\partial t} = \frac{k_c a}{\varepsilon^s(1-\varepsilon^g)\varphi^s}(c_k - c_k^s) + \frac{1}{\varepsilon^s}\sum_{j=1}^{J}\nu_{k,j}R_j, \quad k = 1,\ldots,K \tag{2}$$

Table 1
Reactions on NO_x storage catalyst and the rate laws employed in the model

Reaction step		Reaction rate
$CO + \frac{1}{2}O_2 \rightarrow CO_2$	(1′)	$R_1 = k_1 \frac{y_{CO} y_{O_2}}{G_1}$
$H_2 + \frac{1}{2}O_2 \rightarrow H_2O$	(2′)	$R_2 = k_2 \frac{y_{H_2} y_{O_2}}{G_1}$
$C_3H_6 + \frac{9}{2}O_2 \rightarrow 3CO_2 + 3H_2O$	(3′)	$R_3 = k_3 \frac{y_{C_3H_6} y_{O_2}}{G_1}$
$CO + H_2O \rightleftharpoons CO_2 + H_2$	(4′)	$R_4 = k_4 \left(y_{CO} y_{H_2O} - \frac{y_{CO_2} y_{H_2}}{K^{eq}_{y,4}} \right)$
$C_3H_6 + 3H_2O \rightarrow 3CO + 6H_2$	(5′)	$R_5 = k_5 \left(y_{C_3H_6} y_{H_2O} - \frac{y^3_{CO} y^6_{H_2}}{K^{eq}_{y,5} y^2_{H_2O}} \right)$
$CO + NO \rightarrow CO_2 + \frac{1}{2}N_2$	(6′)	$R_6 = k_6 y_{CO} y^{0.5}_{NO}$
$H_2 + NO \rightarrow H_2O + \frac{1}{2}N_2$	(7′)	$R_7 = k_7 y_{H_2} y^{0.5}_{NO}$
$C_3H_6 + 9NO \rightarrow 3CO_2 + 3H_2O + \frac{9}{2}N_2$	(8′)	$R_8 = k_8 y_{C_3H_6} y^{0.5}_{NO}$
$NO + \frac{1}{2}O_2 \rightleftharpoons NO_2$	(9′)	$R_9 = k_9 \left(y_{NO} y^{0.5}_{O_2} - \frac{y_{NO_2}}{K^{eq}_{y,9}} \right) \frac{1}{G_1}$
$Ce_2O_3 + \frac{1}{2}O_2 \rightarrow Ce_2O_4$	(10′)	$R_{10} = k_{10} \Psi_{cap,O_2} y_{O_2} (\psi^{eq}_{O_2} - \psi_{O_2})$
$Ce_2O_4 + CO \rightarrow Ce_2O_3 + CO_2$	(11′)	$R_{11} = k_{11} \Psi_{cap,O_2} y_{CO} \psi_{O_2}$
$Ce_2O_4 + H_2 \rightarrow Ce_2O_3 + H_2O$	(12′)	$R_{12} = k_{12} \Psi_{cap,O_2} y_{H_2} \psi_{O_2}$
$Ce_2O_4 + \frac{1}{9}C_3H_6 \rightarrow Ce_2O_3 + \frac{1}{3}CO_2 + \frac{1}{3}H_2O$	(13′)	$R_{13} = k_{13} \Psi_{cap,O_2} y_{C_3H_6} \psi_{O_2}$
$2NO_2 + BaCO_3 + \frac{1}{2}O_2 \rightarrow Ba(NO_3)_2 + CO_2$	(14′)	$R_{14} = k_{14} \Psi_{cap,NO_x} y_{NO_2} y^{0.1}_{O_2} (\psi^{eq}_{NO_x} - \psi_{NO_x})$
$2NO + BaCO_3 + \frac{3}{2}O_2 \rightarrow Ba(NO_3)_2 + CO_2$	(15′)	$R_{15} = k_{15} \Psi_{cap,NO_x} y_{NO} y^{0.1}_{O_2} (\psi^{eq}_{NO_x} - \psi_{NO_x})$
$Ba(NO_3)_2 + 5CO \rightarrow N_2 + 5CO_2 + BaO$	(16′)	$R_{16} = k_{16} \Psi_{cap,NO_x} \frac{y_{CO} \psi_{NO_x}}{G_2}$
$Ba(NO_3)_2 + 5H_2 \rightarrow N_2 + 5H_2O + BaO$	(17′)	$R_{17} = k_{17} \Psi_{cap,NO_x} \frac{y_{H_2} \psi_{NO_x}}{G_2}$
$Ba(NO_3)_2 + \frac{5}{9}C_3H_6 \rightarrow N_2 + \frac{5}{3}CO_2 + \frac{5}{3}H_2O + BaO$	(18′)	$R_{18} = k_{18} \Psi_{cap,NO_x} \frac{y_{C_3H_6} \psi_{NO_x}}{G_2}$
$Ba(NO_3)_2 + 3CO \rightarrow 2NO + 3CO_2 + BaO$	(19′)	$R_{19} = k_{19} \Psi_{cap,NO_x} \frac{y_{CO} \psi_{NO_x}}{G_3}$
$Ba(NO_3)_2 + 3H_2 \rightarrow 2NO + 3H_2O + BaO$	(20′)	$R_{20} = k_{20} \Psi_{cap,NO_x} \frac{y_{H_2} \psi_{NO_x}}{G_3}$
$Ba(NO_3)_2 + \frac{1}{3}C_3H_6 \rightarrow 2NO + CO_2 + H_2O + BaO$	(21′)	$R_{21} = k_{21} \Psi_{cap,NO_x} \frac{y_{C_3H_6} \psi_{NO_x}}{G_3}$
$BaO + CO_2 \rightarrow BaCO_3$	(22′)	$R_{22} = \sum_{j=16}^{21} R_j$

$G_1 = (1 + K_{a,1} y_{CO} + K_{a,2} y_{C_3H_6})^2 (1 + K_{a,3} y^2_{CO} y^2_{C_3H_6})(1 + K_{a,4} y^{0.7}_{NO_x}) T$, $G_2 = 1 + K_{a,6} y_{O_2}$, $G_3 = (1 + 0.1 K_{a,6} y_{O_2})(1 + K_{a,7} y_{NO_x})$. Rate laws R_1–R_3 are taken after [13].

$$\frac{\partial \psi_m(z,t)}{\partial t} = \frac{1}{\Psi^{cap}_m} \sum_{j=1}^{J} \nu^{\psi}_{m,j} R_j, \qquad m = 1, \ldots, M \tag{3}$$

$$\rho c_p \frac{\partial T(z,t)}{\partial t} = -v \frac{\partial T}{\partial z} \rho c_p + \frac{k_h a}{\varepsilon^g} (T^s - T) \tag{4}$$

$$\rho^s c^s_p \frac{\partial T^s(z,t)}{\partial t} = \lambda^s \frac{\partial^2 T^s}{\partial z^2} + \frac{k_h a}{(1-\varepsilon^g)} (T - T^s) - \alpha (T^s - T^e) - \varphi^s \sum_{j=1}^{J} \Delta H_{r,j} R_j \tag{5}$$

Boundary conditions at the inlet ($z = 0$) and at the outlet ($z = L$) of the monolith are:

$$T|_{z=0} = T^{in}, \qquad v|_{z=0} = v^{in} \tag{6}$$

$$\left. \frac{\partial T^s}{\partial z} \right|_{z=0} = 0, \qquad \left. \frac{\partial T^s}{\partial z} \right|_{z=L} = 0 \tag{7}$$

$$c_k|_{z=0} = c^{in}_k, \qquad k = 1, \ldots, K \tag{8}$$

The axial coordinate $z = 0$ is located at the monolith inlet and $z = L$ corresponds to the monolith outlet. The inlet gas linear

velocity v^{in} can be calculated from the following equation:

$$v^{in} = \frac{\dot{V}^{in}}{S\varepsilon^{g}} \quad (9)$$

where $\dot{V}$ is the volumetric flow rate, S the frontal area of monolith and ε^{g} is the fraction of open frontal area. Assumptions of negligible moles change, ideal gas, and constant (atmospheric) pressure are used.

Considered set of reactions is defined in Table 1. An effective combination of pseudo-stationary kinetics (reactions (1′)–(9′) and transient kinetics with the explicit consideration of the most important surface-deposited components (reactions (10′)–(22′), the stored oxygen and NO_x) has been applied. The storage phenomena are characterised here by the maximum effective storage capacities ($\Psi_{cap,m}$), temperature dependences of the relative saturation coverages ($\psi_m^{eq}(T)$) and kinetic constants for the storage processes ($k_j(T)$). The parameters are evaluated from dynamic experiments with the catalyst samples in laboratory reactor. This combination enables the simulation of relatively complex chemical system representing the real exhaust gas composition, while keeping the number of individual reaction steps and computation time on reasonable level.

An alternative model, based on more complex microkinetic approach, has been proposed for the limited chemical system [14]. In that model, carbon monoxide and C_3H_6 were employed for the reduction of the stored NO_x. Hydrogen was excluded and the reactions of CO and C_3H_6 with water and CO_2 were neglected, as well as the oxygen storage effects. The use of microkinetic scheme has lead to high demands on computation times [14]. For similarly limited reaction system, another model based on the description of internal diffusion in NO_x storage nano-particles on the catalyst surface has been also proposed [15].

In our model, the reaction rates R_j are related to the volume of active washcoat, defined by φ^{s}—volume fraction of the washcoat (w) in entire solid phase (s)[1]:

$$\varphi^{s} = \frac{V^{w}}{V^{s}} \quad (10)$$

Exponential, Arrhenius-type temperature dependence of kinetic constants is considered:

$$k_j = A_j \exp\left(\frac{-E_{a,j}}{R^{g}T}\right) \quad (11)$$

Spatially dependent external heat and mass transfer coefficients (k_h and k_c, respectively) are calculated from the correlations [16].

Finite differences method with semi-implicit approximations of time derivatives, first-order Taylor's expansion of reaction rates, and adaptive time-step control is used to solve the set of partial differential Eqs. (1)–(5). The model has been implemented in Fortran into XMR software, which forms a part of versatile software package for dynamic simulations of interconnected systems of reactors and adsorbers, being developed at Department of Chemical Engineering, Prague Institute of Chemical Technology [17,12,18–20,22]. On a typical current desktop computer, the computation is approx. 3–15 times faster than the net run of the corresponding experiment.

[1] The solid phase consists of inert substrate and active washcoat.

3. Arrangement of experiments and evaluation of kinetic parameters

Dynamic behaviour of several industrial NO_x storage catalyst samples was examined experimentally. The studied catalysts were of the type NM/Ba/CeO_2/γ-Al_2O_3 washcoated on 400 cpsi cordierite monolith. Other active components (e.g., surface stabilisers and secondary NO_x storage components) were also present in the washcoat. The maximum effective NO_x storage capacity varied among individual samples in the range 200–1400 mol NO_x per m^3 washcoat, due to different loading of active NO_x storage components. The results given in this paper were obtained for the catalyst with lower NO_x storage capacity (360 mol NO_x per m^3 of washcoat). Qualitatively the same phenomena were observed for all the studied catalysts.

Experiments have been carried out in nearly isothermal, modular steel micro-reactor, containing three (identical) small monolith samples in series [17]. The size of each sample was 3 cm × 3 cm × 0.5 cm. Temperature was measured in front of and behind each sample. For experiments with highly exothermic rich mixtures, temperature increase was not negligible. The actual measured values were then considered in simulations and evaluation of kinetic parameters. Inlet gas temperature in the course of experiments was 100–550 °C. Experiments were performed either with constant inlet temperature at 150, 200, 250, . . ., 550 °C (storage experiments, lean/rich switching), or with the slowly increasing temperature ramp (light-off experiments). The reaction mixture was prepared on-line from individual synthetic gases, representing the most important components in automobile exhaust gas: CO, O_2, C_3H_6, H_2, NO, CO_2 and H_2O, which were admixed to N_2 (carrier gas). Concentrations of the individual components were continuously set by fast mass-flow controllers. The flow rate

Table 2
Conditions used in the experiments and simulations (inlet gas composition is given in mol. fractions)

Variable	Lean phase	Rich phase
GHSV (h^{-1})	30000	30000
T^{in} (°C)	100–550	100–550
y^{in}_{NO} (ppm)	150	150
$y^{in}_{NO_2}$ (ppm)	0–150	0
$y^{in}_{O_2}$ (%)	7	0–1.6
$y^{in}_{CO_2}$ (%)	10	10
$y^{in}_{H_2O}$ (%)	10	10
y^{in}_{CO} (%)	0.25	0.5–4.5
$y^{in}_{C_3H_6}$ (ppm)	200	0–7000
$y^{in}_{H_2}$ (%)	0.05	0.5–3.5
$y^{in}_{N_2}$	Balance	Balance

was GHSV = 30 000 h^{-1} and the inlet gas always contained 10% H_2O and 10% CO_2.[2] The conditions used in the experiments and simulations are summarised in Table 2. On-line IR absorption analysers (ABB Advanced Optima Uras) were employed for CO, CO_2, NO, and NO_x measurements in the outlet gas, while the O_2, HC and H_2 concentrations were analysed by mass spectrometer (Pfeiffer Vacuum Omnistar GSD301).

Pre-treatment of fresh catalyst samples was 1 h on stream at 500 °C, lean (oxidising) conditions and then 1 h lean/rich operation at 300 °C. After that, no change of catalyst activity or storage capacity was observed in the course of experimental series. Prior to each NO_x storage measurement, the stored NO_x were removed from the catalyst by the reduction using CO, H_2 and C_3H_6 at 400 °C. The sample was then cooled down to the temperature of experiment and inlet gas containing 7% O_2, 10% H_2O and 10% CO_2 was introduced for several minutes before the start of experiment.

The experiments were focused on the evaluation of model reaction kinetic parameters necessary for the prediction of NO_x storage catalyst behaviour under typical lean/rich operation—$k_j(T)$, $K_{a,j}(T)$, $\Psi_{cap,m}$ and $\psi_m^{eq}(T)$; cf. Table 1. A minimum set of experiments has been proposed: (i) CO, H_2 and HC oxidation light-off under both lean and rich conditions, including inhibition effects, (ii) NO/NO_2 transformation, (iii) NO_x storage, including temperature dependence of effective NO_x storage capacity, (iv) water gas shift and steam reforming under rich conditions, i.e., *in situ* production of hydrogen, (v) oxygen storage and reduction, including temperature dependence of effective oxygen storage capacity, and (vi) NO_x desorption and reduction under rich conditions.

The described sequence of the studied reactions was followed also in the gradual process of kinetic parameters evaluation, so that the number of simultaneously optimised kinetic parameters was always kept on a low level. For example, for the evaluation of the rich-phase NO_x desorption and reduction, the following reaction rates have to be determined beforehand: CO, H_2 and HC oxidation, water gas shift and steam reforming, oxygen storage and reduction, and NO_x storage capacity. The evaluation of kinetic parameters was based on the comparison of the experimental data with the model predictions, employing adaptive simplex optimisation method and weighted least-squares objective function.

4. Results and discussion

The function of NSRC converter is based on the NO_x storage and the consequent reduction. However, the other reactions taking place in the system (cf. Table 1) have to be also considered, particularly to evaluate the balance of reductants in the rich phase, temperature effects, and efficiency of the enrichment with respect to NO_x reduction. Reactions of particular interest are CO, H_2 and HC oxidation by oxygen (including oxygen storage effects) and water (cf. reactions (1′)–(5′), (11′)–(13′) in Table 1). Examples of light-off experiments for CO and C_3H_6 oxidation are given in Fig. 1(a and b) for different conditions—the effects of lean versus rich composition (i.e., the self-inhibition by high CO and HC concentrations) and the inhibition by NO can be clearly seen. The observed light-off temperatures for the individual reductants were always in the order $H_2 < CO < C_3H_6$ at corresponding conditions. The developed model with optimised kinetic

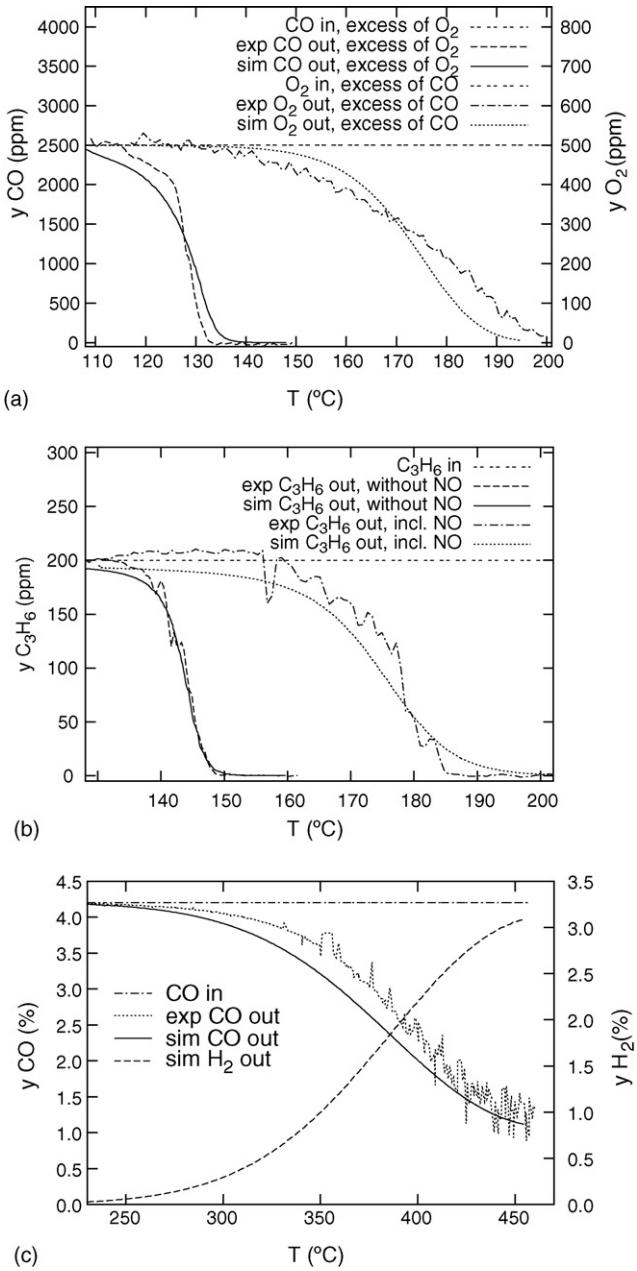

Fig. 1. Experimentally observed and simulated light-off curves. (a) CO oxidation—influence of lean (excess of O_2) and rich (excess of CO) conditions. Composition of inlet gas (mol. fractions)—lean mixture: 0.25% CO, 7% O_2; rich mixture: 0.25% CO, 0.05% O_2; both mixtures: 0 ppm NO, 0 ppm HC, 0 ppm H_2. (b) C_3H_6 oxidation—influence of inhibition by NO. Composition of inlet gas (mol. fractions): 200 ppm C_3H_6, 0.25% CO, 7% O_2, 0 ppm H_2, and 0 or 150 ppm NO. (c) Water gas shift—production of hydrogen, compostion of inlet gas (mol. fractions): 4.2% CO, 0 ppm HC, 0 ppm O_2, 0 ppm NO, 0 ppm H_2. All gas mixtures: 10% H_2O, 10% CO_2, balance N_2. Temperature ramp, 3 K min^{-1}.

[2] Throughout this paper, the concentrations are given in mole fractions.

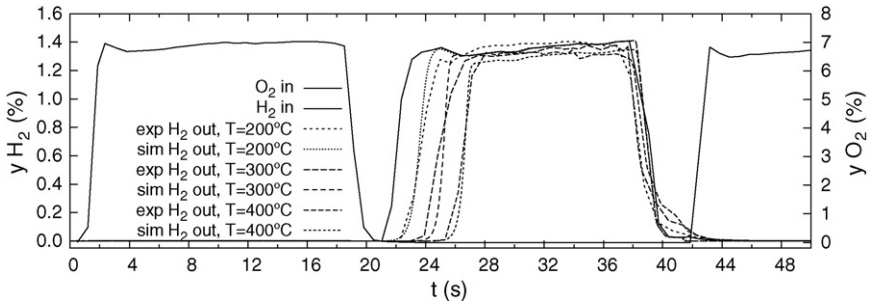

Fig. 2. Experimentally observed and simulated oxygen storage and reduction. Composition of inlet gas (mol. fractions)—lean mixture: 7% O_2, 0% H_2; rich mixture: 1.4% H_2, 0% O_2; both mixtures: 0 ppm NO, 0 ppm CO, 0 ppm HC, 10% H_2O, 10% CO_2, balance N_2.

parameters $k_1(T)$–$k_3(T)$ and $K_{a,1}(T)$–$K_{a,5}(T)$ was able to describe large variations of reaction rate and light-off temperature under studied conditions.

Water gas shift and steam reforming reactions producing H_2 under rich conditions (reactions (4′) and (5′) in Table 1, respectively), start to be significantly active at the temperatures above 300 °C (cf. Fig. 1c). These reactions result in different actual $CO:C_3H_6:H_2$ concentration ratio inside the monolith in comparison with the set composition of rich inlet gas mixture. The reactions are characterised by the kinetic parameters $k_4(T)$ and $k_5(T)$, as well as by the thermodynamic equilibrium constants ($K_{y,4}^{eq}$ and $K_{y,5}^{eq}$).

Even if the aim if the NO_x storage catalyst preparation is to minimise the oxygen storage effects (to efficiently utilise the excess of CO, H_2 and HC in the rich phase for the NO_x reduction), it is practically impossible to produce the catalyst with zero oxygen storage capacity since cerium oxides are used for the stabilisation of the washcoat structure [23]. Experiments with step changes between oxygen and individual reductants (CO, H_2, and C_3H_6) were performed at different temperatures to study the oxygen storage effects (cf. reactions (10′)–(13′) in Table 1). As can be seen in Fig. 2, the effective oxygen storage capacity increases monotonously with temperature, which is in agreement with other experimental observations [24]. At higher temperatures, the amount of reductants consumed during the rich phase by the reactions with the stored oxygen cannot be neglected. From these experiments, the model parameters Ψ_{cap,O_2}, $\psi_{O_2}^{eq}(T)$ and $k_{10}(T)$–$k_{13}(T)$ are evaluated.

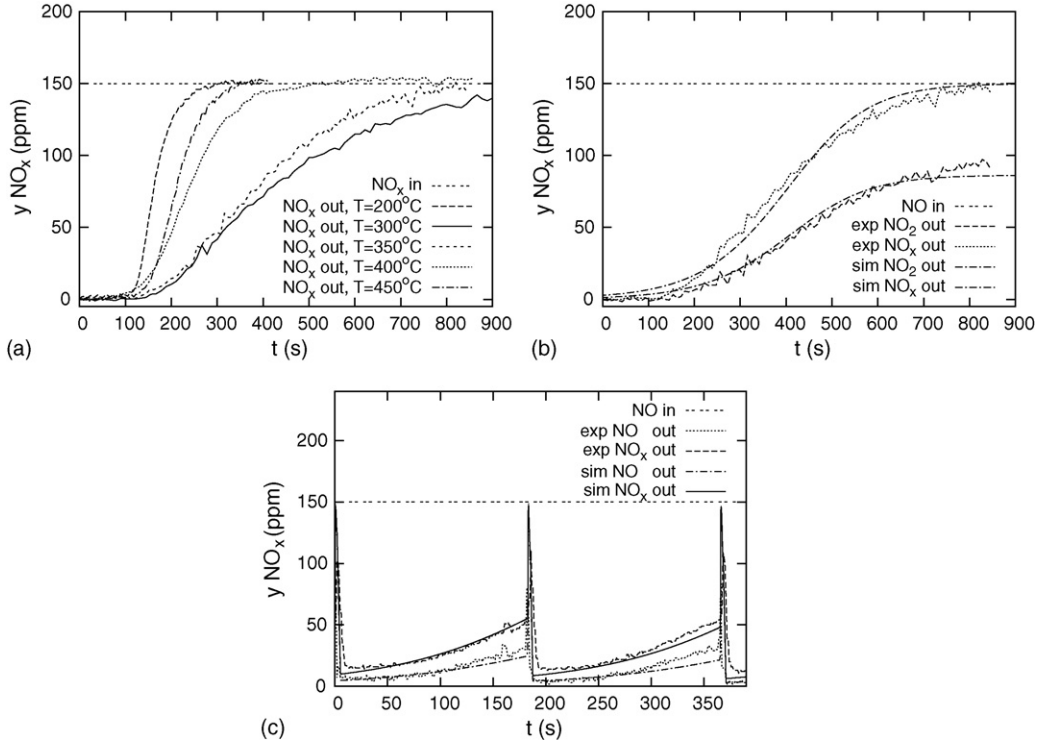

Fig. 3. (a) Examples of isothermal NO_x adsorption curves, measured at different temperatures. (b) Experimentally observed and simulated NO_x concentrations in the course of NO_x adsorption at 350 °C. Inlet gas composition during adsorption experiments (mol. fractions): 150 ppm NO, 7% O_2, 10% H_2O, 10% CO_2, balance N_2. (c) Experimentally observed and simulated outlet NO_x concentrations in the course of periodic lean/rich operation at 350 °C. Lean phase 180 s, rich phase 2 s. Lean inlet mixture: 7% O_2, 200 ppm C_3H_6, 0.25% CO, 0.05% H_2. Rich inlet mixture: 1.6% O_2, 4.2% CO, 1.4% H_2, 7000 ppm C_3H_6. Both mixtures also contain: 150 ppm NO, 10% H_2O, 10% CO_2, balance N_2.

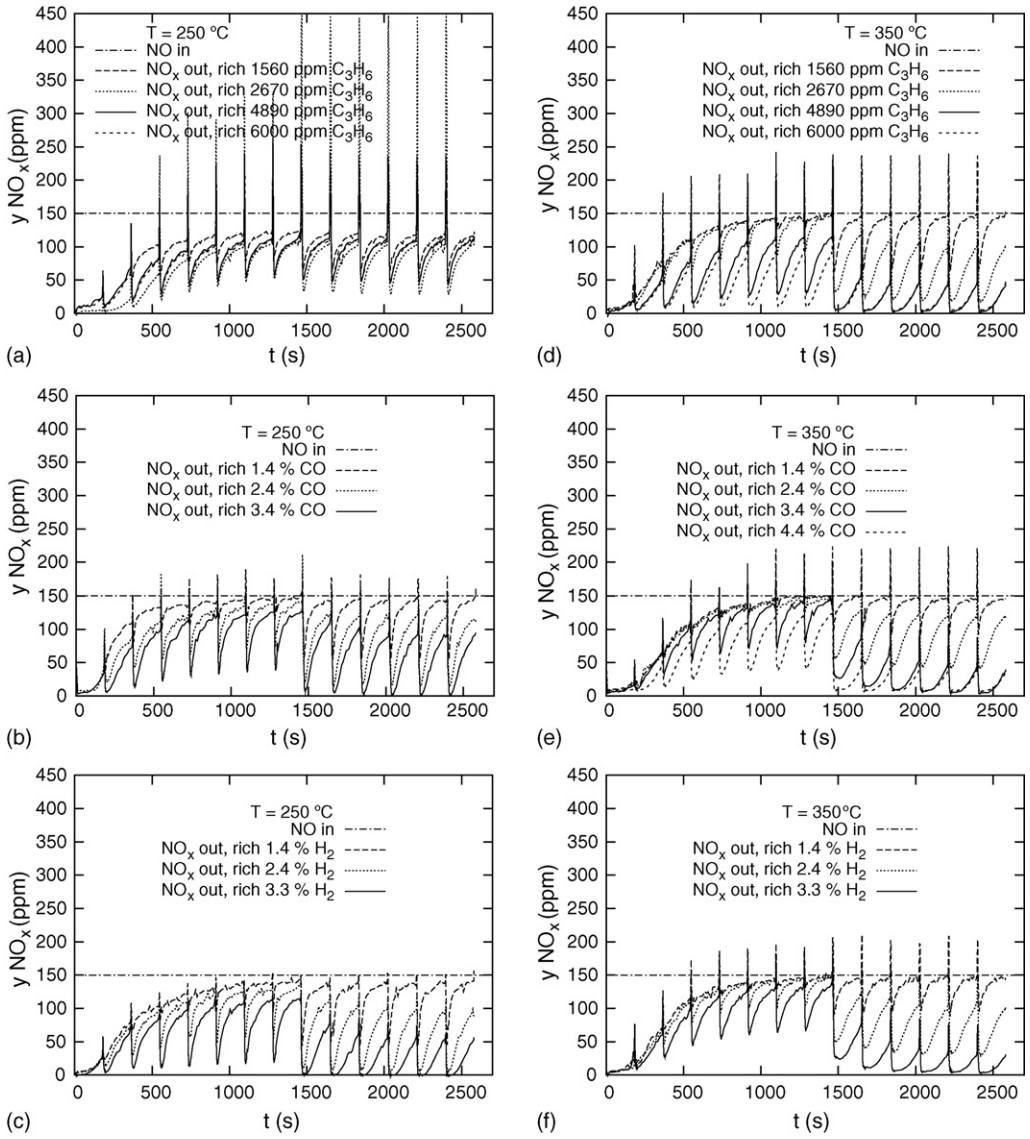

Fig. 4. NO_x storage and reduction experiments—effects of composition and length of rich phase on periodic lean/rich operation at two different temperatures: lower temperature T^{in} = 250 °C (a–c) and higher temperature T^{in} = 350 °C (d–f). Applied reductants: C_3H_6 (a and d), CO (b and e), and H_2 (c and f). In all cases lean phase 180 s, rich phase 2 s (1st to 7th period) and 6 s (8th to 14th period). Lean inlet mixtures: 7% O_2, 0.25% CO (a and d) or 0.05% H_2 (b and e) or 200 ppm C_3H_6 (c and f). Rich inlet mixtures: 0.2% O_2, for reductant concentrations cf. labels in (a–f). All mixtures (a–f, both lean and rich) also contain: 150 ppm NO, 10% H_2O, 10% CO_2, balance N_2.

Temperature dependence of the effective NO_x storage capacity was studied by isothermal NO adsorption experiments (at T = 150, 200, 250,. . ., 550 °C) in the presence of O_2, CO_2 and H_2O (cf. Fig. 3). The values of the effective NO_x storage capacity are decomposed into constant value of maximum capacity (Ψ_{cap,NO_x}, mol m^{-3} washcoat) and relative, temperature-dependent equilibrium NO_x saturation $\psi^{eq}_{NO_x}(T)$ from the interval $\langle 0,\ 1\rangle$. This approach allows to describe the NO_x storage in a wide temperature range. The maximum effective NO_x storage capacity corresponds to $\psi^{eq}_{NO_x} = 1$. The maximum is observed at intermediate temperatures around 300 °C, which is in agreement with the previous results published for this reaction system—cf., e.g., [3,5,6], the review [10] and additional references given there. Temperature dependence of the effective NO_x storage capacity reflects the complex nature of the processes on the catalyst surface, influenced by the competitive chemisorption of other gases (CO_2, H_2O), different temperature stabilities of the individual chemisorbed species, transformation of the forms of the stored NO_x (nitrites, nitrates), the presence of different types of NO_x storage sites, and the internal diffusion effects [10].

The values Ψ_{cap,NO_x} and $\psi^{eq}_{NO_x}(T)$ are calculated from the integral balance of the gas-phase NO_x over the adsorption experiment (time interval $<t_0, t_1>$). For the total volume of the monolith samples V, the fraction of open frontal area ε^g, the fraction of washcoat in the solid phase φ^s and the constant flow rate F (in moles), the balance is

$$\Psi_{cap,NO_x}\psi^{eq}_{NO_x}(T) = \frac{F}{V(1-\varepsilon^g\varphi^s)}\int_{t_0}^{t_1}(y^{in}-y^{out})\,dt \qquad (12)$$

The kinetic constants of the NO_x storage process $k_{14}(T)$ and $k_{15}(T)$ are then evaluated from the time course of the adsorption curves. The reversible transformation of NO to NO_2 is also followed in dependence on temperature and the kinetic parameter $k_9(T)$ is evaluated, considering the thermodynamic equilibrium limitation $K^{eq}_{y,9}$. Comparison of simulated and experimentally observed evolution of the outlet NO_x and NO_2 concentrations is given in Fig. 3(b). The effects of CO_2 and H_2O on the NO_x storage process (cf. [10]) were implicitly included—the both gases were always present in the model gas mixtures, similarly as they inhere in the real exhaust gas. In a typical periodic lean/rich operation, the enrichment resulting in NO_x reduction is applied well before complete NO_x breakthrough, so that high overall NO_x conversions can be achieved (cf. Fig. 3(c)).

Kinetic parameters $k_{16}(T)$–$k_{21}(T)$ of the NO_x desorption and reduction are evaluated from the experimental study of periodic lean/rich operation at different temperatures, with varying length and composition of the rich phase. Experimental results obtained at 250 and 350 °C are depicted in Fig. 4. The concentrations of reductants were chosen on the basis of stoichiometric equivalence (1 mol $C_3H_6 \approx 9$ mol CO ≈ 9 mol H_2, cf. also Table 1). Certain similarities can be seen for all the experiments: At the start, there are no NO_x adsorbed on the surface. Rather short enrichment (2 s) is applied during the first to seventh lean/rich period, so that the reduction of the accumulated NO_x is incomplete and outlet NO_x concentrations gradually increase. After few periods, the lean/rich operation is stabilised. Then, in the 8st to 14th period, the longer enrichment (6 s) is applied, which improves the reduction of the stored NO_x and results in the decrease of the average outlet NO_x concentrations.

The course of the lean/rich experiment is documented by the simulated evolution of the surface NO_x concentrations, which is depicted in Fig. 5. It can be seen that during the operation with the shorter rich phase, the unreduced surface NO_x accumulate particularly in the rear part of the monolith series (i.e., the last catalyst sample), where the lowest concentration of reductants is met during the enrichment. Application of the longer rich phase (the second part of the experiment) results in almost complete reduction of the stored NO_x and improved outlet NO_x conversions.

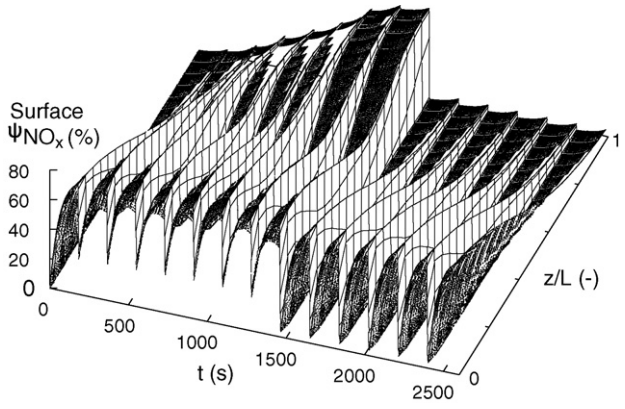

Fig. 5. Computed spatiotemporal concentration profile of the stored NO_x in the course of periodic lean/rich operation, corresponding to 350 °C and 4.4% CO (rich) in Fig. 4(e). Prediction of the model, z/L is dimensionless spatial coordinate along the series of monolith samples (0 = inlet of the first sample, 1 = outlet of the last sample) and ψ_{NO_x} is relative surface coverage of NO_x storage sites.

The extent of NO_x reduction increases with the concentration of reductant and the rich-phase length until the limit of complete NO_x reduction is achieved. The obtained dependences of the surface NO_x reduction on the rich-phase length and composition form a basis for the evaluation of the stored NO_x desorption and reduction rates using individual reductants ($k_{16}(T)$–$k_{21}(T)$ in Table 1). At the lower temperature (250 °C, Fig. 4(a)–(c)), the NO_x reduction is slower and less effective—no complete reduction is observed even for the longer rich phase with high reductant concentrations. The catalyst temperature is only slightly above the light-off (for rich conditions) and under such conditions the differences between individual reductants can be clearly seen. The observed order of activity ($H_2 > CO > C_3H_6$) corresponds with the experimental results obtained by other researchers [25,10]. It can be seen in Fig. 4(a) that also the lean NO_x reduction by C_3H_6 takes place in the system – although only in a limited extent – which decreases the steady-state outlet NO_x concentrations under lean conditions.

At the higher temperature, the rich-phase NO_x reduction is much faster and more extensive (compare Fig. 4(d)–(f) with Fig. 4(a)–(c)). Practically complete reduction of the stored NO_x can be observed in Fig. 4(d) and (e) for the 6 s rich phase and higher concentrations of the reductants. Furthermore, the evolution of the outlet NO_x concentrations at the higher temperature is less sensitive to the type of reductant. Two reasons for this effect can be identified: (i) mass transport limitations (particularly internal diffusion) for the highly transient processes of the NO_x desorption and reduction, and (ii) the transformation of C_3H_6 and CO into H_2 by the reactions of CO and C_3H_6 with water (cf. Table 1 and Fig. 1(c)). For the employed effective 1D model, the internal diffusion effects are implicitly included in the evaluated kinetic parameters. More detailed models of catalytic monolith with the explicit consideration of internal diffusion can be also employed (cf., e.g., [20–22,26]), however, longer computation times are then demanded.

5. Conclusions

Spatially 1D, heterogeneous mathematical model of NO_x storage catalytic monolith was developed. It is designed to effectively describe and quantify the most important effects taking place in the course of typical periodic operation of NO_x storage and reduction catalysts in automobiles—catalyst light-off for CO, H_2 and HC oxidation including inhibition effects, water gas shift and steam reforming reactions, temperature-dependent oxygen and NO_x storage, and the effects of rich-phase length and compostion (CO, H_2 or HC). Minimum set of experiments necessary for the evaluation of relevant reaction-kinetics parameters was discussed. Typical examples of the experimental results were given and compared with the

simulation results. The developed model forms a useful tool for the prediction of NO_x storage converter performance under varying conditions and different monolith configurations.

Acknowledgements

The work was supported by Czech Grant Agency (grant 104/05/2616) and Czech Ministry of Education (project MSM 6046137306).

References

[1] N. Takahashi, H. Shinjoh, T. Iijima, T. Suzuki, K. Yamazaki, K. Yokota, H. Suzuki, N. Miyoshi, S. Matsumoto, T. Tanizawa, T. Tanaka, S. Tateishi, K. Kasahara, Catal. Today 27 (1996) 63.
[2] http://www.dieselnet.com2005.
[3] L. Lietti, P. Forzatti, I. Nova, E. Tronconi, J. Catal. 204 (2001) 175.
[4] P. Broqvist, H. Grönbeck, E. Fridell, I. Panas, Catal. Today 96 (2004) 71.
[5] W.S. Epling, J.E. Parks, G.C. Campbell, A. Yezerets, N.W. Currier, L.E. Campbell, Catal. Today 96 (2004) 21.
[6] R.L. Muncrief, P. Khanna, K.S. Kabin, M.P. Harold, Catal. Today 98 (2004) 393.
[7] Y. Su, M.D. Amiridis, Catal. Today 96 (2004) 31.
[8] J. Dawody, M. Skoglundh, L. Olsson, E. Fridell, J. Catal. 234 (2005) 211.
[9] H.Y. Huang, R.Q. Long, R.T. Yang, Appl. Catal. B 33 (2001) 127.
[10] W.S. Epling, L.E. Campbell, A. Yezerets, N.W. Currier, J.E. Parks, Catal. Rev. 46 (2004) 163.
[11] S. Kojima, N. Baba, S. Matsunaga, K. Senda, K. Katoh, T. Itoh, SAE Technical Paper 2001-01-1297 (2001).
[12] J. Jirát, M. Kubíček, M. Marek, Catal. Today 53 (1999) 583.
[13] S. Voltz, C. Morgan, D. Liederman, S. Jacob, Ind. Eng. Chem. Prod. Res. Dev. 12 (1973) 294.
[14] L. Olsson, E. Fridell, M. Skoglundh, B. Andersson, Catal. Today 73 (2002) 263.
[15] U. Tuttlies, V. Schmeißer, G. Eigenberger, Chem. Eng. Sci. 59 (2004) 4731.
[16] K. Ramanathan, V. Balakotaiah, D.H. West, Chem. Eng. Sci. 58 (2003) 1381.
[17] http://www.vscht.cz/monolith2005.
[18] J. Jirát, M. Kubíček, M. Marek, Chem. Eng. Sci. 56 (2001) 1597.
[19] P. Kočí, M. Kubíček, M. Marek, T. Maunula, M. Härkönen, Chem. Eng. J. 97 (2004) 131.
[20] P. Kočí, M. Kubíček, M. Marek, Ind. Eng. Chem. Res. 43 (2004) 4503.
[21] P. Kočí, M. Kubíček, M. Marek, Catal. Today 98 (2004) 345.
[22] D. Kryl, P. Kočí, M. Kubíček, M. Marek, T. Maunula, M. Härkönen, Ind. Eng. Chem. Res. 44 (2005) 9524.
[23] J. Kašpar, P. Fornasiero, N. Hickey, Catal. Today 77 (2003) 419.
[24] M. Boaro, F. Giordano, S. Recchia, V. Dal Santo, M. Giona, A. Trovarelli, Appl. Catal. B 52 (2004) 225.
[25] H. Abdulhamid, E. Fridell, M. Skoglundh, Top. Catal. 30/31 (2004) 161.
[26] P. Kočí, F. Štěpánek, M. Kubíček, M. Marek, Chem. Eng. Sci. 61 (2006) 3240.